Physica B 694 (2024) 416456

Contents lists available at ScienceDirect

Physica B: Condensed Matter

journal homepage: www.elsevier.com/locate/physb

Effects of annealing temperature, doping concentration, and excitation wavelength on photoluminescence characteristics of GdOCl:Bi^{3+} phosphor powders

Babiker M. Jaffar [a], Nadir A.M. Saeed [b], R.E. Kroon [b], Rudolph M. Erasmus [a], Odireleng Martin Ntwaeaborwa [c,*]

[a] School of Physics, University of the Witwatersrand, 1 Jan Smuts Avenue, Johannesburg, South Africa
[b] Department of Physics, University of the Free State, Box 339, Bloemfontein, 9300, South Africa
[c] Department of Physics, Sol Plaatje University, Kimberley, 8300, South Africa

ARTICLE INFO

Keywords:
GdOCl
Bismuth
Photoluminescence
Stability
Quantum yield

ABSTRACT

This study presents a novel investigation of the structure, particle morphology and photoluminescence (PL) characteristics of $Gd_{1-x}OCl:Bi_x$ phosphors prepared by a solid-state reaction method. X-ray diffraction data confirmed the formation of the tetrahedral GdOCl phase. The phosphors emitted peculiar photoluminescence that was dependent on the excitation wavelength, annealing temperature and doping concentration. When undoped GdOCl host was excited at 275 nm, a narrowband ultraviolet B (UVB) was observed at 315 nm. This emission is ascribed to the $^8S_{7/2} \rightarrow {}^6I_J$ transition of Gd^{3+}. After doping with Bi^{3+}, two excitation bands were observed at 275 nm (major excitation) and 336 nm (minor excitation). Exciting Bi^{3+} doped GdOCl at 275 and 366 nm resulted in two broad emission bands at 455 nm (bluish green) and 428 nm (blue) ascribed to and $^3P_{0,1} \rightarrow {}^1S_0$ transitions of Bi^{3+}. The PL peak intensities of these emissions were found to vary with Bi^{3+} doping concentrations and annealing temperatures. The decay characteristics and photoluminescence quantum yield of the blue photoluminescence were determined, and the mechanism of the blue Bi^{3+} emission is proposed.

1. Introduction

In the field of luminescent materials, phosphors are of paramount importance due to their ability to convert absorbed energy into visible emission within the wavelength range of 380–700 nm. Their diverse applications range from illuminating sources like fluorescent lamps, white light-emitting diodes, and X-ray intensifying screens. They also find extensive use in optoelectronic devices, displays, and scintillators [1,2]. Research in advanced phosphors with enhanced photoluminescence properties is crucial for the growing demand of energy-efficient and high-performance lighting devices.

One intriguing class of phosphor materials is rare earths (RE) oxychlorides (REOCl), known for their excellent luminescent properties [3–5]. Among these materials, gadolinium oxychloride (GdOCl) is an excellent host lattice due to its unique crystal structure and optical properties [5]. Ease of incorporation of rare-earths dopant ions in the GdOCl lattice sites is necessary for production of advanced phosphor materials that can be used in different types of light emitting displays.

Rare earth ions are often introduced as activators in various host lattices. For instance, the GdOCl host has been doped with rare earth activators such as Tm^{3+} and Yb^{3+} [6], Ce^{3+}, Tb^{3+}, Eu^{3+}, Dy^{3+}, Sm^{3+}, Ho^{3+}, and Er^{3+} to develop diverse phosphor materials [7–10] that emit light in a wide spectral range. Moreover, other metal ions like Ti^{+}, Pb^{2+}, Sb^{3+}, and Bi^{3+} have also been used as activators [11] in various host lattices such as LaOCl and GdOCl to prepare phosphors. The incorporation of Sb^{3+} into LaOCl was reported by Van Steensel et al. [12], and they observed blue and green emissions ascribed to secluded clusters of Sb^{3+} ions in the host lattice sites and grain boundaries, respectively. Wolfert et al. investigated the luminescent characteristics of LnOCl (Ln = La, Y, Gd) activated Bi^{3+} and observed two distinct emissions bands in the ultraviolet and visible spectral regions [13].

In this study, we investigated the effects of annealing temperature, excitation wavelengths, and Bi^{3+} doping concentrations on the photoluminescence properties of $Gd_{1-x}OCl:Bi_x$. GdOCl has been chosen as a host lattice because of its unique structural and chemical properties. Furthermore, the GdOCl's layered crystal structure provides a controlled

* Corresponding author.
E-mail address: martin.ntwaeaborwa@spu.ac.za (O.M. Ntwaeaborwa).

https://doi.org/10.1016/j.physb.2024.416456
Received 11 July 2024; Received in revised form 17 August 2024; Accepted 24 August 2024
Available online 24 August 2024

synthesis, modification platform and a favourable environment for hosting dopants such as rare earth ions or transition metals. This characteristic sets it apart from other gadolinium-based host lattices like Gd_2O_3 and $GdCl_3$. Furthermore, GdOCl exhibits characteristics optical and electronic properties making it suitable for use in displays, scintillators, and photocatalysis applications. Its wide bandgap makes it particularly attractive for easy of incorporation of rare-earths dopants like Bi^{3+} and many more.

GdOCl crystallizes in the tetragonal PbFCl-type structure, with space group *P4/nmm* (No. 129) [6]. The crystal structure illustrated in Fig. 1 was modeled utilizing Vesta software [14] with input from the CIF (crystallographic information framework) file sourced from Springer Materials. The Gd^{3+} ions exhibit a 4-coordinate geometry within this arrangement, forming bonds with four equivalent O^{2-} ions and five equivalent Cl^- ions. The Gd–O bond lengths measure 2.28 Å uniformly, while Gd–Cl recorded one shorter bond length at 3.07 Å and four longer bonds lengths at 3.10 Å. The O^{2-} ions are connected to four equivalent Gd^{3+} ions, generating a combination of edge and corner-sharing OGd_4 tetrahedra. The Cl^- ions adopt a 5-coordinate geometry, forming bonds with five equivalent Gd^{3+} atoms [15]. In Fig. 1(b), the Gd^{3+} atom exhibits square antiprismatic coordination geometry. In this arrangement, five chlorine atoms make up one of the square faces, while the other square face is formed by four oxygen atoms [1].

Phosphors activated by Bi ions exhibit intriguing and diverse luminescent properties, primarily attributed to favourable interaction between Bi ions and the surrounding host lattice atoms. This interaction is strong because the outer s^2 electron orbital of Bi ion is not shielded from the electrostatic fields of the surrounding environment [16]. Additionally, numerous valence states of Bi ions contribute to these distinctive luminescent behaviours. Typically, phosphor materials incorporating Bi^{3+} ions emit light in the near-ultraviolet and blue spectral ranges. Researchers have extensively explored the luminescent properties of Bi^{3+} ions in various host lattices [17].

The ground state of the Bi^{3+} free ion is made up of the $^1S_0$ energy state of the $6s^2$ electronic configuration, while the excited 6s6p configuration contains four crystal field-split $^3P_0$, $^3P_1$, $^3P_2$, and $^1P_1$ states. The optical transition from $^1S_0 \rightarrow {}^3P_0$ and $^1S_0 \rightarrow {}^3P_2$ are usually spin-orbit forbidden. However, the $^1S_0 \rightarrow {}^3P_2$ electron transition occur via coupling with unsymmetrical lattice vibrational modes. The $^1S_0 \rightarrow {}^1P_1$ and $^1S_0 \rightarrow {}^3P_1$ transitions are spin-orbit allowed [17].

This study explores and discusses the crystal structure and spectroscopic properties GdOCl:Bi^{3+} powders. The effects of Bi^{3+} doping concentration, annealing temperature, and excitation wavelength on photoluminescent properties of the powders are reported. A simplified energy level diagram that explains the mechanism of photon absorption and photoemission is presented.

2. Experimental

Gadolinium oxychloride (GdOCl) powder samples were prepared using the solid-state reaction method. The reaction for the formation of GdOCl is given by the following equation:

$$Gd_2O_3 + 2NH_4Cl \rightarrow 2GdOCl + 2NH_3 + H_2O \quad (1)$$

The intended molar ratio of Gd_2O_3 to NH_4Cl was 1:2, but a 25 % excess of NH_4Cl was utilized during the synthesis process. Before weighing, the Gd_2O_3 powder was heated for 4 h at 800 °C in air to make it more stable and prevent conversion to $Gd(OH)_3$.

For the synthesis of GdOCl, 1.082 g of Gd_2O_3 and 0.4011 g of NH_4Cl both, both from Sigma-Aldrich with 99.999 % purity, were combined in 10 mL of acetone. The mixture was thoroughly ground using an agate mortar and pestle. The resulting powder blend was transferred to a porcelain crucible and annealed at temperatures ranging from 500 °C to 900 °C for 1 h in ambient atmospheric conditions.

To prepare Bi-doped samples, appropriate quantities of Gd_2O_3, NH_4Cl, and Bi_2O_3 (99.999 % purity, were mixed using a mortar and pestle and the same procedure as above was followed.

X-ray diffraction (XRD) analysis was conducted utilizing a Rigaku MiniFlex600 diffractometer to examine the crystal structure of the materials. The X-ray source was operated with the electron beam current of 15 mA at 40 kV to generate Cu Kα characteristic X-rays. The diffuse reflectance spectroscopy (DRS) analysis was conducted using a Varian Cary 500 UV–Vis–NIR spectrophotometer equipped with Harrick Scientific Praying Mantis™ Diffuse Reflection Accessory.

Photoluminescence data were obtained utilizing a Horiba QM8000 spectrofluorometer equipped with dual excitation and emission monochromators. A monochromatized xenon lamp served as the excitation source, while signal detection from the sample was facilitated by a PPD-850 Si photodiode detector. Emission correction was applied to the as-recorded data. Time-correlated single photon counting (TCSPC) measurements of lifetimes were done using a Horiba NanoLED source, exciting at 266 nm, equipped with a photodiode detector. The data was acquired using the FelixGS software. Raman data were acquired utilizing a Horiba LabRAM HR Raman spectrometer equipped with an Olympus BX41 microscope accessory. The excitation source used was the 514.5 nm line generated by a Lexel 95-SHG argon ion laser. The incident beam

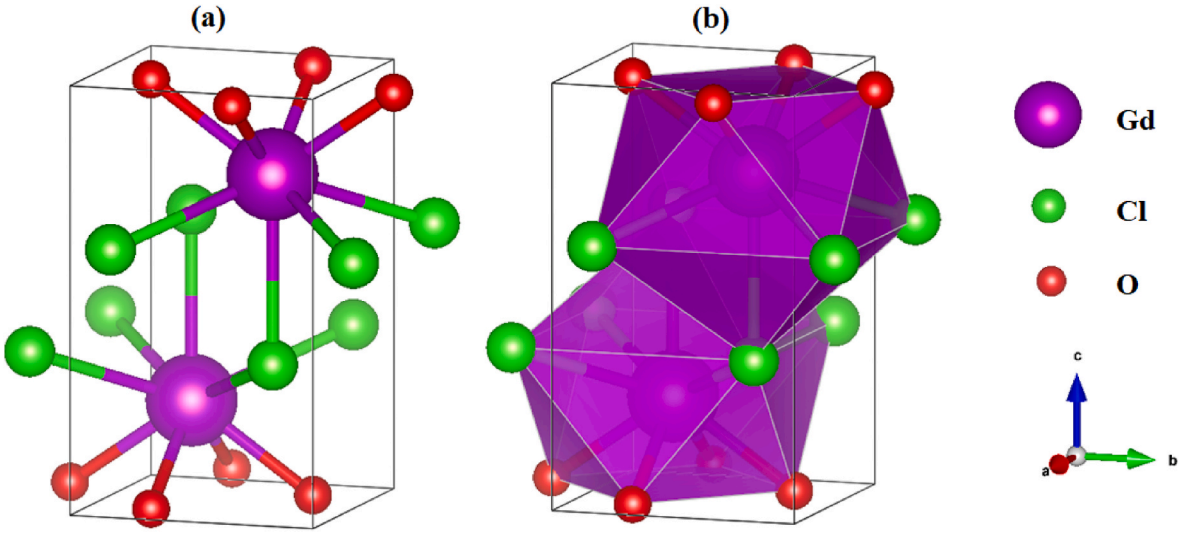

Fig. 1. (a) Crystal structure of GdOCl and (b) the coordination geometry of the Gd^{3+} ion in a square antiprismatic arrangement, modeled utilizing Vesta software [14] with input from the CIF file sourced from Springer Materials.

was focused onto the sample via a 100 × objective lens (N.A. = 0.90). The backscattered signal was dispersed via a 600 lines/mm grating onto a CCD detector cooled by liquid nitrogen, with acquisition performed using LabSpec v5 software. The investigation of particle morphologies was conducted utilizing a Zeiss Sigma 03–39 Field Emission Scanning Electron Microscope (FE-SEM) from Zeiss, Oberkochen, Germany, operating at an accelerating voltage of 30 kV. The elemental composition was also evaluated through energy-dispersive X-ray spectroscopy (EDS). Quantum yield measurements were carried out using an Edinburgh FLS980 instrument with an integrating sphere.

3. Results and discussion

3.1. Structure, morphology, and chemical composition analysis

Fig. 2 (a) shows the XRD patterns of GdOCl host samples that were annealed at temperatures ranging from 500 to 900 °C in ambient air for 1 h. The patterns are compared with the standard reference data for GdOCl with the tetragonal PbFCl-type crystal structure (JCPDS card no. 00-012-0798) and the space group *P4/nmm* (No. 129). For the samples annealed at 500 °C–800 °C, all the diffraction peaks are consistent with the standard data file, confirming the formation of the homogenous phase of the tetragonal GdOCl crystal structure [6]. However, for the sample annealed at 900 °C, there are additional peaks (marked with asterisks *) pointing to the formation of the secondary phase of Gd_2O_3 in the material composition. The results showed that there is phase transition when annealing at temperatures above 800 °C (see Fig. 3).

Fig. 2 (b) depicts the XRD patterns, measured in the range of 10°–80°, for $Gd_{1-x}OCl:Bi_x$ annealed at 700 °C. These samples were activated with varying concentrations of Bi^{3+} (x = 0, 0.000, 0.001, 0.005, 0.010, 0.015, 0.020, and 0.025). After doping, no additional diffraction peaks were detected, signifying the successful incorporation of Bi^{3+} ions into the GdOCl lattice sites. It is most likely that Bi^{3+} (ionic radius = 1.31 Å) substituted Gd^{3+} (ionic radius = 1.247 Å) due to similarities in their ionic radii [18]. The Williamson–Hall equation (2) was used to determine the average crystallite size *D* and microstrains (ε) for the $Gd_{1-x}OCl:Bi_x$ (x = 0.000, 0.001, 0.005, 0.010, 0.015, 0.020, and 0.025) samples:

$$\beta \cos\theta = \frac{K\lambda}{D} + 4\varepsilon \sin\theta \quad (2)$$

where β is the 2θ full-width-at-half-maximum (in radians) for the diffraction peak at the angle θ, *K* is the shape factor (taken as 0.94), λ is the X-ray wavelength, *D* is the crystallite size and ε is the microstrain [19]. The values are presented in Table 1, and the show that the average crystallite size for both the undoped and Bi^{3+}-doped GdOCl remained nearly was approximately 75 nm irrespective of the doping concentration.

The Rietveld refinement process was used to refine the structural parameters using powder X-ray diffraction data with the help of The FullProf software [20]. The refinement process focused on optimizing several key parameters including the background, scale factor, global thermal factor, profile half-width parameters (u, v, w), asymmetric factor, site occupancy factors (Wyckoff), and structural parameters (a, c). This refinement was intended to enhance the quality and reliability of the structural data. Fig. 4 presents the XRD patterns for GdOCl and GdOCl:Bi, showcasing the observed, calculated, and differences in the patterns. Notably, there is correlation between the calculated and experiment data, confirming a successful crystallisation of the tetragonal GdOCl structure. The refined structural parameters obtained through the Rietveld analysis for undoped GdOCl and $Gd_{1-x}OCl:Bi_{x\ =\ 0.015}$ are shown in Table 2. We did not detect any changes in the cell volume or structural parameters upon conducting analogous Rietveld refinements for other compositions. This can be attributed to similar ionic radii of both Bi^{3+} (1.31 Å) and Gd^{3+} (1.247 Å) [18].

Raman spectroscopy was used to analyze the phonon vibrational frequencies for undoped GdOCl and $Gd_{1-x}OCl:Bi_{x\ =\ 0.015}$ samples. Fig. 5 depicts the Raman spectra for both samples, depicting five out of six possible lines corresponding to frequency modes represented by $2A1_g + 3E_g + B1_g$. The five prominent bands at 118, 180, 235, 375, and 508 cm^{-1} are notably consistent with the findings reported in Ref. [8]. This alignment with prior research further confirms the formation of the tetragonal GdOCl structure. Notably, the Raman spectrum of the Bi-doped GdOCl sample closely resembled that of the undoped host.

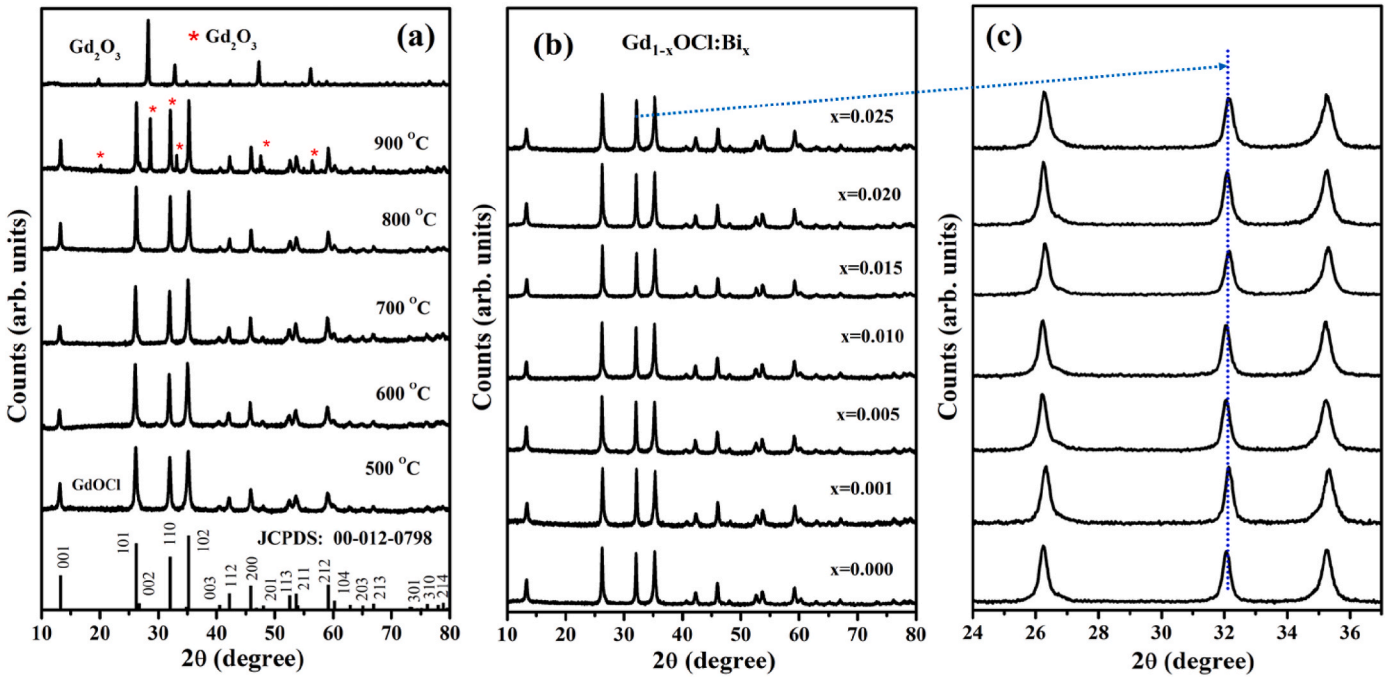

Fig. 2. XRD patterns for GdOCl (a) annealed at various temperatures, together with information from JCPDS card #00-012-0798, and (b) GdOCl activated with various Bi concentrations annealed at 700 °C (c) Magnified view of the 101, 110, 102 diffraction peaks for doped samples.

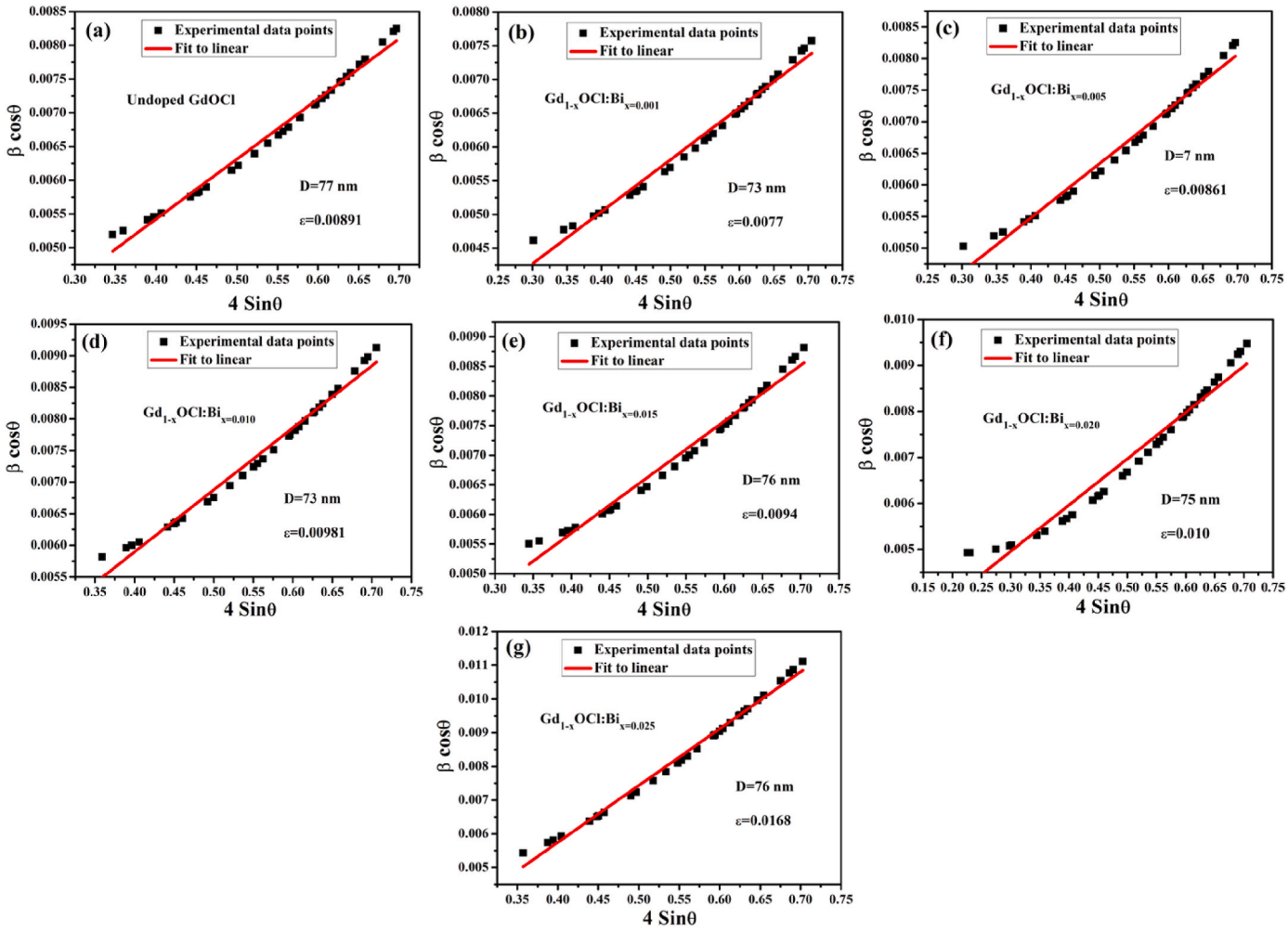

Fig. 3. Williamson–Hall plots for $Gd_{1-x}OCl:Bi_x$ (x = 0.000, 0.001, 0.005, 0.010, 0.015, 0.020, and 0.025) phosphor powders.

Table 1
Determination of Crystallite Sizes using the Williamson–Hall Equation.

concentrations of Bi (x)	Average crystallite size (nm)	micro-strain
0	77	0.00891
0.001	73	0.00770
0.005	72	0.00861
0.010	73	0.00981
0.015	76	0.00940
0.020	75	0.01010
0.025	76	0.01680

Additionally, as illustrated in Fig. 5, the phonon cutoff energy for GdOCl is approximately 508 cm^{-1}, which is smaller than that of GdOBr (~522 cm^{-1}) [21] and Gd_2O_3 (~600 cm^{-1}) [22].

Fig. 6 illustrates the SEM microphotographs for (a) GdOCl and (b) $Gd_{1-x}OCl:Bi_{x\ =\ 0.015}$, which were annealed at 700 °C in air for 1 h. The samples were prepared by depositing small quantities of powders on double-sided tapes. The powders were not coated with gold. The images reveal a distinct transformation in particle morphology, transitioning from randomly oriented flat thin plates in the undoped GdOCl host to nanorods after incorporating Bi^{3+} dopant ions.

The EDS spectrum obtained from the $Gd_{1-x}OCl:Bi_{x\ =\ 0.015}$ sample (Fig. 7) conclusively verifies the existence of all constituent elements within our material, which include Gd, O, Cl, and Bi. Traces of Cu from the grids on which the samples were mounted and the adventitious C were also observed.

3.2. Diffuse reflectance spectra

The diffuse reflectance spectroscopy (DRS) technique was used to investigate the absorption properties of both the undoped and Bi^{3+}-doped GdOCl host and the spectra are presented in Fig. 8. The reflectance spectrum of the GdOCl host reveals multiple absorption peaks in the UV range. The absorption band below 215 nm which indicates the absorption beyond the band gap, was observed in the undoped sample (Fig. 8 (a)). The absorption peaks at 250, 275, 315 nm are attributed to the 4f-4f transitions of Gd^{3+}, and these absorptions are assigned to the $^8S_{7/2} \rightarrow {}^6D_J, {}^6I_J, {}^6P_J$ transitions of Gd^{3+}, respectively [23].

In the case of the $Gd_{1-x}OCl:Bi_x$ samples, the reflectance spectra reveal two absorption bands positioned approximately at 257 and 337 nm. The absorption peak intensities show a small increase with increasing concentrations of Bi dopants. Analysis of the PL excitation spectra (seen in Fig. 11) suggests that the shorter wavelength absorption peak around 257 nm is linked to the absorption of Bi^{3+}. The longer wavelength absorption peak at approximately 337 nm might be attributed to defects induced by Bi clusters.

To calculate the band gap for the undoped host lattice, the Kubelka-Munk equation, given as $(R_\infty) = \frac{(1-R_\infty)^2}{2R_\infty}$, was utilized to convert the DRS into absorption proportional values [24]. For materials like GdOCl with an indirect band gap [25], the band gap can be determined by plotting $[F(R_\infty)h\nu]^{1/2}$ against hν, where hν represents the photon energy. This involves fitting a linear region and extrapolating to where it intersects the horizontal axis [26]. Such a plot is illustrated in Fig. 8 (c), and the

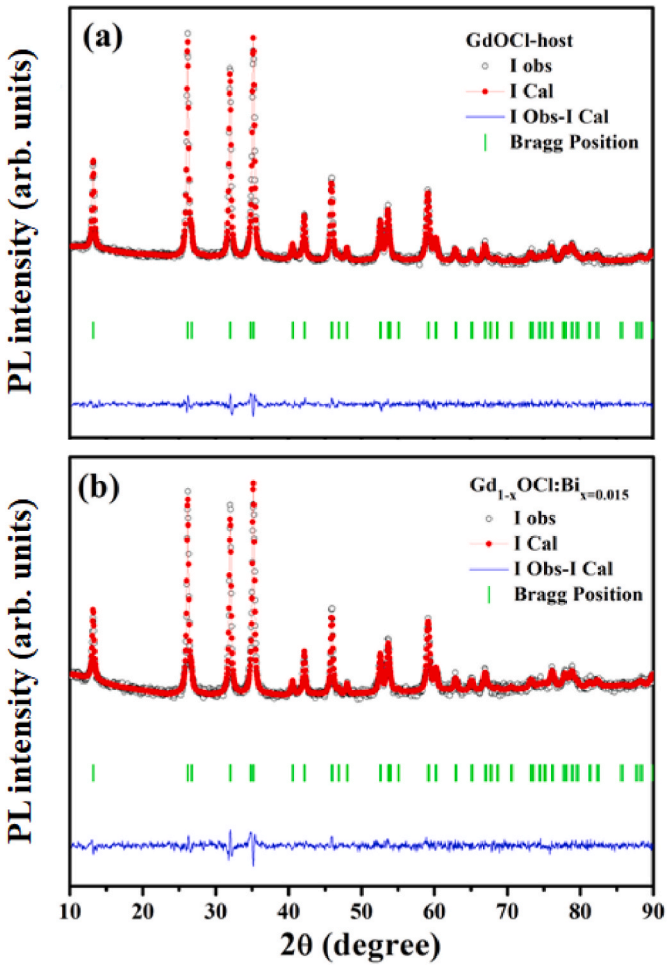

Fig. 4. XRD refinement of (a) undoped GdOCl, and (b) $Gd_{1-x}OCl:Bi_{x\ =\ 0.015}$.

Table 2
The structural parameters obtained from XRD patterns for both the undoped GdOCl host material and the $Gd_{1-x}OCl:Bi_{x\ =\ 0.015}$ phosphor powders. (R_p, R_{wp}, and R_{exp} represent the Bragg-intensity, weighted profile, and statistically expected values, respectively).

Parameters	GdOCl pure host			$Gd_{1-x}OCl:Bi_{x\ =\ 0.015}$
Crystal system	tetragonal			tetragonal
Space group	*P4/nmm*			*P4/nmm*
a (Å)	3.96151			3.95951
c (Å)	6.68495			6.68786
V (Å^3)	104.911			104.850
R_b (%)	16.5			24.0
R_{wp} (%)	12.1			16.3
R_{exp} (%)	6.44			8.58
Atomic positions	x	y	z	occupation
Gd/Bi	0.25	0.25	0.17171	0.62249
Cl	0.25	0.25	0.62243	0.55942
O	0.75	0.25	0	0.41048

optical band gap of the GdOCl host as estimated to be 4.84 eV. In a prior study by Q. Chen et al. [27], the electronic band gap for the undoped GdOCl host was calculated to be 4.74 eV. Discrepancies in the band gap values could be due to variations in preparation methods, different particle morphologies, defects and perhaps the choice of linear fit range. The estimated optical band gap values for $Gd_{1-x}OCl:Bi_x$ at x = 0.001 and x = 0.015 were determined to be 3.52 eV and 2.50 eV, respectively. As the concentration of Bi increased, the band gap value decreased. It is well known that doping alters the electronic arrangement and introduces extra energy states within the bandgap with a subsequent decrease of the bandgap.

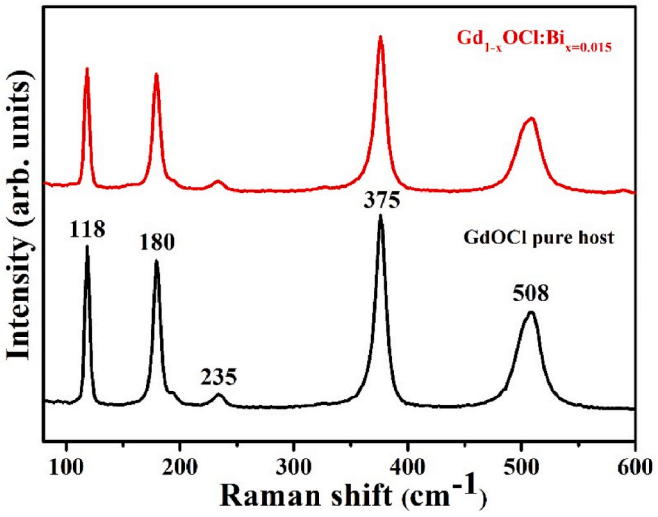

Fig. 5. Raman spectra for (a) GdOCl pure host (b) $Gd_{1-x}OCl:Bi_{x\ =\ 0.015}$.

3.3. PL analysis

Fig. 9 (a) illustrates the PL excitation and emission spectra corresponding to $Gd_{1-x}OCl:Bi_{x\ =\ 0.015}$ samples subjected to varying annealing temperatures. The emission spectra were recorded under excitation at a wavelength of 275 nm. Fig. 9 (b) exhibits the PL emission intensity plotted against annealing temperature, encompassing the range of 500 °C–800 °C. The PL emission intensity rises with increasing annealing temperatures, reaching its peak at 700 °C, then decreasing with further increase in temperature. This observed increase in emission intensity with annealing temperature was expected due to enhanced crystallinity and the reduction of defects. Jafer et al. [28] studied the effect of annealing temperature on Bi-activated Y_2O_3 phosphor powders. They attributed the increase in emission intensity with annealing temperature to the dopant's segregation effects on the particle surface. In contrast, the luminescence quenching at higher annealing temperatures was likely due to desorption of dopant ions from the surface. Moreover, in their study, Jaffar et al. [29] explored the influence of annealing temperature on $LaGaO_3$-doped Bi^{3+}. Their findings revealed a decreased of Bi^{3+} content as the heat treatment temperature increased. Blasse and Bril [30] explored the photoluminescence properties of GdOCl doped with bismuth and ascribed the reduction in emission intensity at elevated temperatures to energy transfer from Bi^{3+} to Gd^{3+}.

Fig. 10 shows the excitation and emission spectra of the undoped GdOCl host, which has been annealed at 700 °C in ambient air for 1 h. The excitation spectrum exhibits distinct peaks at 244 and 254 nm, attributed to the excitation from the $^8S_{7/2}$ to ^6D_J electronic states of Gd^{3+}. Additionally, a peak at 275 nm is attributed to the excitation from the $^8S_{7/2}$ to ^6I_J electronic state of Gd^{3+}, as reported in Ref. [31].

When excited at 275 nm, GdOCl gives two distinct emission peaks with maxima at 315 and 620 nm. The emission peak at 315 nm originates from the $^6P_{7/2}$ to $^8S_{7/2}$ transition of Gd^{3+}. The weak emission centered at 620 nm is attributed to the $^6G_{7/2}$ to $^6P_{3/2}$ transition of Gd^{3+} ions, as reported in Ref. [32]. The narrowband emission at 315 nm is commonly known as ultraviolet B (UVB) and is used in phototherapy lamps to treat various skin diseases.

Fig. 11(a) presents the steady-state photoluminescence excitation spectra of $Gd_{1-x}OCl:Bi_x$, with varying bismuth content, measured when monitoring the 455 nm emission. Three distinct peaks at 240, 275, and 336 nm were detected. The peak at 336 nm aligns with the absorption peak of the Bi dopant, consistent with the diffuse reflectance data

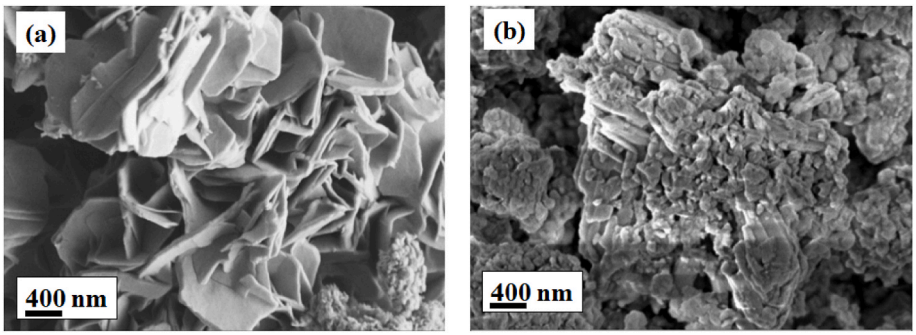

Fig. 6. SE - SEM images of (a) GdOCl pure host and (b) $Gd_{1-x}OCl:Bi_{x\ =\ 0.015}$ annealed at 700 °C for 1h.

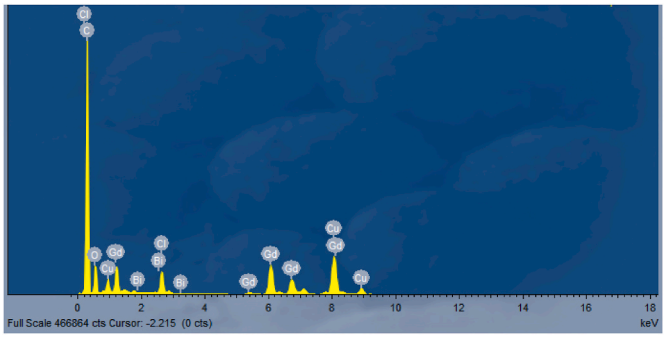

Fig. 7. EDS spectra of $Gd_{1-x}OCl:Bi_{x=0.015}$ phosphor powder.

depicted in Fig. 8 (b). When the samples were excited at 275 nm (Fig. 11 (b)), a broad blueish green emission band extending from 300 to 800 nm and peaking at 455 nm was detected. On the other hand, when excited at 336 nm (as depicted in Fig. 11 (c)), a broad blue emission band was observed, covering the range from 370 to 700 nm, and a maximum at 428 nm. Fig. 11 (d) shows plots of the maximum emission intensity versus Bi concentration for excitation at 275 and 336 nm. Generally, the highest peak intensities for all the doping concentrations of Bi^{3+} were observed when exciting at 275 nm. When exciting at 336 nm, the sample with the lowest bismuth concentration (x = 0.005) exhibits the maximum emission intensity and the PL intensities decreased above this concentration due to concentration quenching effects. However, when exciting at 275 nm, the emission remains consistently stronger, with the maximum intensity at x = 0.015. This concentration (x = 0.015) was identified as the optimal bismuth doping concentration for our samples. The PL emission intensity decreased above this concentration due to the concentration quenching phenomenon, which occurs due to energy migration between the dopants ions as a result of electric dipole or quadrupole interactions. Significant quenching may occur for low dopant concentrations ranging from 0.001 to 0.025 mol% [33], indicating a strong interaction among the Bi^{3+} ions.

The positioning of the excitation and emission peaks originating from Bi^{3+} is contingent upon the specific host lattice in which they are embedded. Three distinct excitation bands have been identified, each exhibiting a unique central wavelength: 240, 275, and 336 nm. The excitation wavelength at 336 nm aligns with the absorption peak of the Bi, as depicted in Fig. 8(b).

The 336 nm excitation is ascribed to the transitions from the $^1S_0$ to the $^3P_1$ level. In comparison, the relatively feeble excitation at 240 nm could potentially be attributed to either the $^1S_0$ to $^1P_1$ transition, known as the C band, or the occurrence of metal-to-metal charge transfer (MMCT) interactions between the Bi^{3+} ions and the Gd^{3+} cations within the host material.

To gain deeper insights into the origins of these excitation bands, Wang and colleagues [34] established a practical correlation among the energy levels associated with the A band ($^1S_0 \rightarrow {}^3P_1$) and the C band ($^1S_0 \rightarrow {}^1P_1$). This relationship is expressed as $E_C = 3.236 + 2.290(E_A - 2.972)^{0.856}$, with energy values provided in (eV). When considering the A band excitation transitions for GdOCl:Bi occurring at 336 nm, the corresponding energy prediction for the C band is 4.93 eV (250 nm). This value is slightly lower than the observed higher energy excitation peak at 240 nm (5.16 eV).

Alternatively, one can estimate the energy associated with MMCT between Bi^{3+} and Gd^{3+} cations within the host material using the formula $E_{MMCT} = 55\,000–45\,500\chi/d$ (in cm^{-1}) [35]. Here, χ represents the electronegativity of the host cations, and d is the distance between Bi^{3+} and host cations measured in angstroms (Å).

By using $\chi = 1.33$ for GdOCl from Ref. [35] and $d_{GdOCl} = 4.83$ Å (see Fig. 1), the MMCT excitation energy for GdOCl:Bi is expected to be around 42471 cm^{-1}, which is approximately equivalent to 235 nm (5.27 eV). This value is close to the higher energy excitation band at 240 nm (5.16 eV) measured in this work. The higher energy excitation band at 240 nm is probably the result of the C and MMCT bands. In previous study [36], established the MMCT between Bi^{3+} ions and La^{3+} cations in LaOCl and LaOBr hosts occurred at 250 nm.

To further justify our findings, it is useful to predict the accurate position of the A band based on the excitation difference. This will allow us to make an accurate suggestion of the position of the MMCT with respect to the A band. Theoretically, we can predict the position of the A band based on the environmental factor (h_e). This factor contains important information about the chemical bond, including the covalence, bond volume polarization, the ligand's charge in the chemical bond, and the central ion's coordination number. The position of the A band can be calculated using the following equation [37]:

$$E_A\ (X, cm^{-1}) = 23970 + 50051\ \exp(-h_e / 0.551) \quad (3)$$

here, E_A is the position of the A band in cm^{-1}. The literature value of h_e of GdOCl is 1.271 [38]. The predicted A band was determined theoretically to be 28954 ± 3000 cm^{-1} (345 ± 25 nm, 3.6 ± 0.5 eV). This value has a difference $|E_{exp}(Bi^{3+}) - E_A(X)|$ equal to 720 cm^{-1}, whereas the difference $|E_{exp}(Bi^{3+}) - E_{MMCT}(Bi^{3+})|$ is equal to 13517 cm^{-1}. This allows us to relate the deconvoluted peak at 3.68 eV to the A band, with the MMCT band lying above the A band. It is also useful to analyze the nature of the emission bands based on the Stokes shift according to the model that was suggested by Amer and Boutinaud [39]. The model $|E_{MMCT}(Bi^{3+}) - E_A(X) - \Delta stokes|$ suggested that the maximum Stokes shift energy difference of about 4000 cm^{-1} is related to the A band emitters. Similarly, the lowest energy difference for MMCT is about 7500 cm^{-1}. Considering the excitation and emission for A band, E_A (X, cm^{-1}) = 28954 cm^{-1} (345 nm), E_{MMCT} = 42471 cm^{-1} (235 nm), and the Stokes shift ($\Delta stokes$ = 6310 cm^{-1}), the energy difference is about 7207 cm^{-1}. Similarly, if we apply the same argument considering the second excitation and emission, the energy difference for E_{ex} = 36364 cm^{-1} (275 nm) and (14386 cm^{-1}) is about 8279 cm^{-1}. According to this model, the differences of 7207 cm^{-1} and 8279 cm^{-1} suggest both

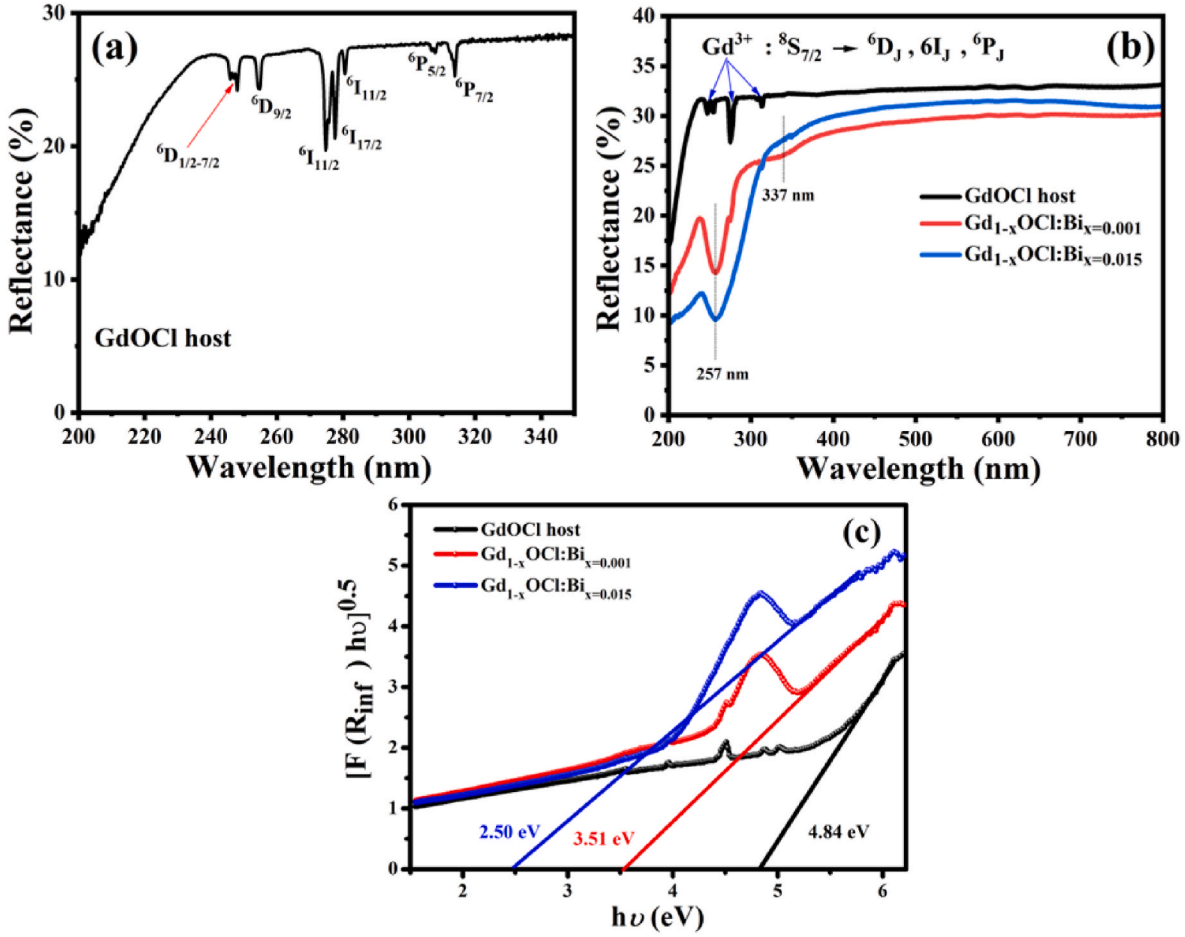

Fig. 8. Diffuse reflectance spectra of (a) undoped GdOCl (b) undoped GdOCl and $Gd_{1-x}OCl:Bi_x$ doped samples. (c) A Tauc plot to determine energy band gaps for the undoped and Bi^{3+} - doped GdOCl samples.

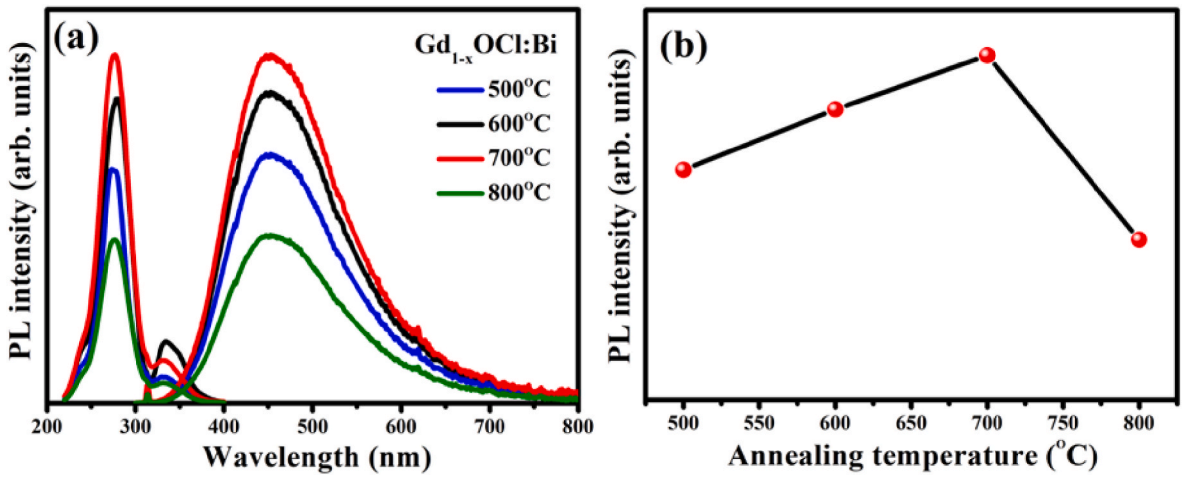

Fig. 9. (a) Excitation and emission spectra of $Gd_{1-x}OCl:Bi_{x\ =\ 0.015}$, annealed at different temperatures. (b) Emission peak intensity as a function of annealing temperature.

emissions are related to D-like emitters (Bi^{3+} to transition metal charge transfer). In particular, the energy difference of 7207 cm^{-1}, lies between the maximum of the A band emitters and the lower edge of the D band emitters. This was due to the large Stokes shift of the D emitters, accompanied by the large Frank-Condon offset and large force constant of the coinciding excited potential curve. Also, the D level can be populated from the lower laying level, surpassing the energy barrier dividing the two levels. Consequently, for a specific temperature, the efficiency of the process, $\left|E_{MMCT}\left(Bi^{3+}\right) - E_A(X)\right|$, relies on the lattice vibrational energy and the excited state relaxation [39]. This behaviour is similar to that of $La_2Zr_2O_7:Bi^{3+}$ [40].

With the fact that the nature of the excitation at 275 nm is ambiguous and GdOCl has only one site to be occupied by Bi^{3+} ions, the determined differences for both excitations and emissions are more complicated and

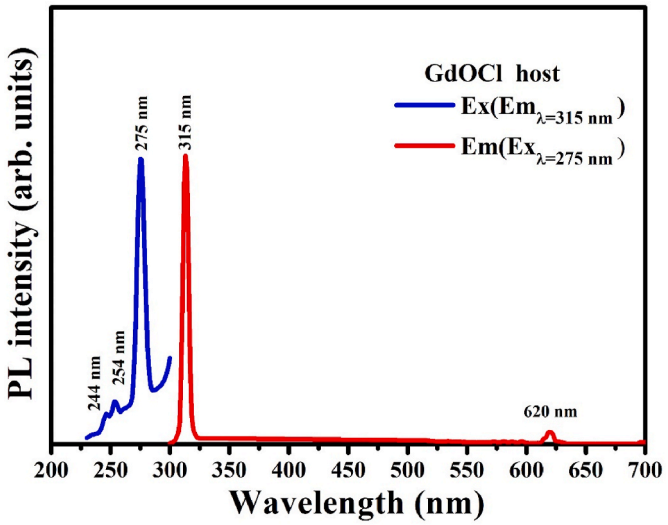

Fig. 10. PL spectra for GdOCl pure host.

motivated us to consider the effect of the presence of Gd^{3+} ions in our system. The Gd^{3+} excitation and emission depicted in Fig. 10 showed the main excitation of Gd^{3+} at about 275 nm, whereas the emission in the 300–500 nm range contained different transitions of Gd^{3+}. We suggest that the excitation at 275 nm is a contribution from Gd^{3+} and Bi^{3+} ions. This agrees with the suggestion made by Wolfert and Blasse [30].

The emission band peaking at 455 nm, as depicted in Fig. 11 (b), is ascribed to the $^3P_1 \rightarrow {}^1S_0$ transition of Bi^{3+} in GdOCl. When the sample was excited at 337 nm, as presented in Fig. 11 (c), the resulting emission displayed two peaks in the visible region. Due to the challenge of precisely determining the positions of the weaker, longer wavelength peaks, Gaussian fitting (as shown in Fig. 12) was employed. The fitted peaks were identified at 379 nm (3.27 eV) and 492 nm (2.52 eV). It is well-known that LaOCl:Bi exhibits dual emission peaks, one in the ultraviolet region and the other in the visible spectrum. The ultraviolet emission peak is ascribed to the $^3P_1 \rightarrow {}^1S_0$ transition of the Bi^{3+}, while the peak in the visible region is attributed to the clustering of Bi [30,36].

Fig. 13 depicts a simplified energy level diagram illustrating electronic transitions of Bi^{3+} based on the data acquired in this investigation. The band gap, calculated from diffuse reflection data, is 4.84 eV. The bottom of the $^1S_0$ level is set as the reference (zero) level. The curve representing the $^3P_1$ energy level is positioned within the band gap, with its minimum offset to ensure alignment with the experimental excitation and emission data between the $^1S_0$ and $^3P_1$ levels (measured at 4.50 eV and 2.7 eV, respectively). Furthermore, the $^1P_1$ band is at its anticipated 4.93 eV (~251 nm).

The CCT or correlated color temperature indicates light's cool or warm characteristics. The evaluation of CCT is facilitated using CIE coordinates (x, y) of the phosphors, employing McCAMY's formula. The equation to determine the CCT is [41]:

$$CCT = 449n^3 + 3525n^2 + 6823.3n + 5520.33 \quad (4)$$

Where $n = \frac{(x-0.330)}{(0.1858-y)}$ and (x, y) represents the calculated CIE coordinates of the selected samples. Fig. 14 illustrates the chromaticity coordinates and the CCT values of $Gd_{1-x}OCl:Bi_x$ phosphor powders annealed at 700 °C for 1 h in air. The $Gd_{1-x}OCl:Bi_x$ phosphor powders are blue when excited at either 275 nm or 336 nm wavelength. The CCT

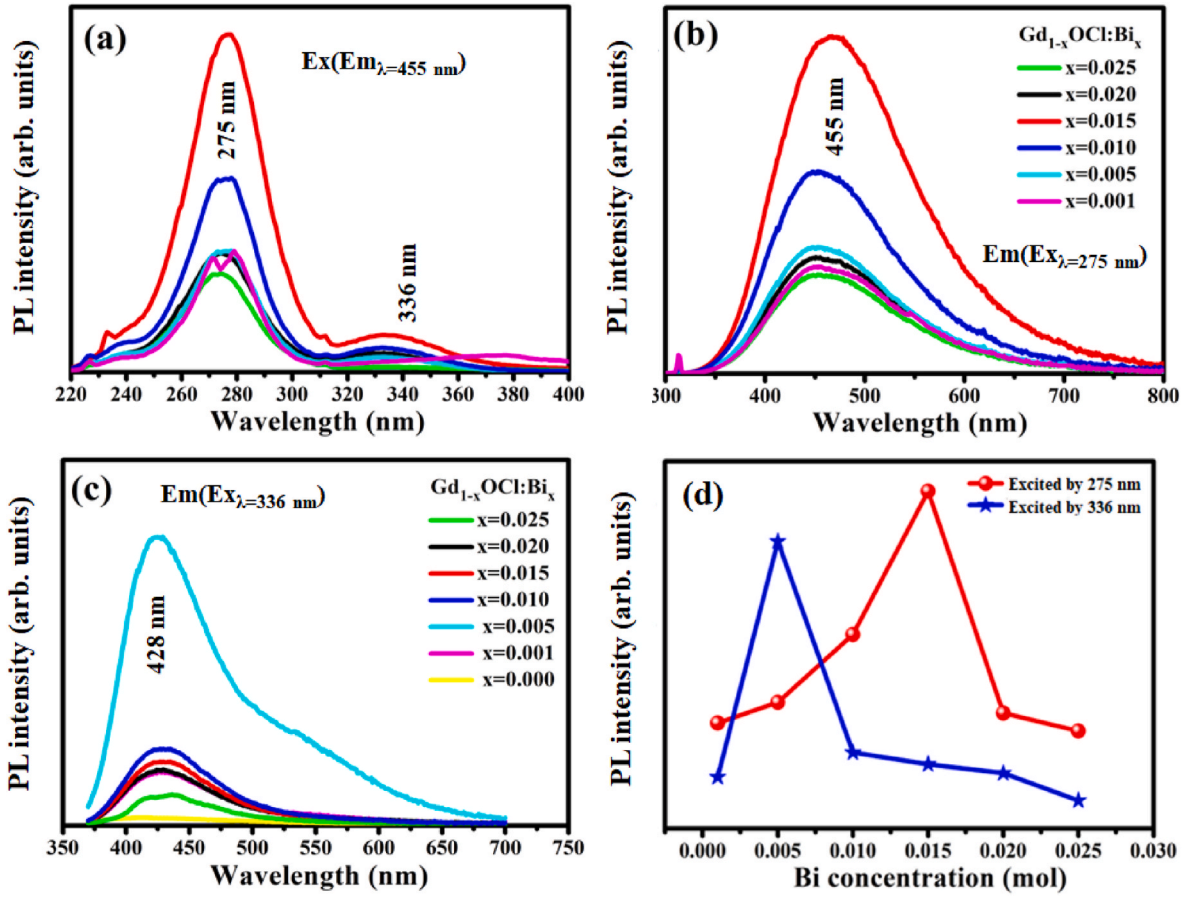

Fig. 11. (a) Excitation spectra of $Gd_{1-x}OCl:Bi_x$ activated with varying concentrations of Bi^{3+} ions. PL emission spectra correspond to (b) excitation at 275 nm and (c) excitation at 337 nm. (d) Variation in emission peak intensity plotted against Bi concentration.

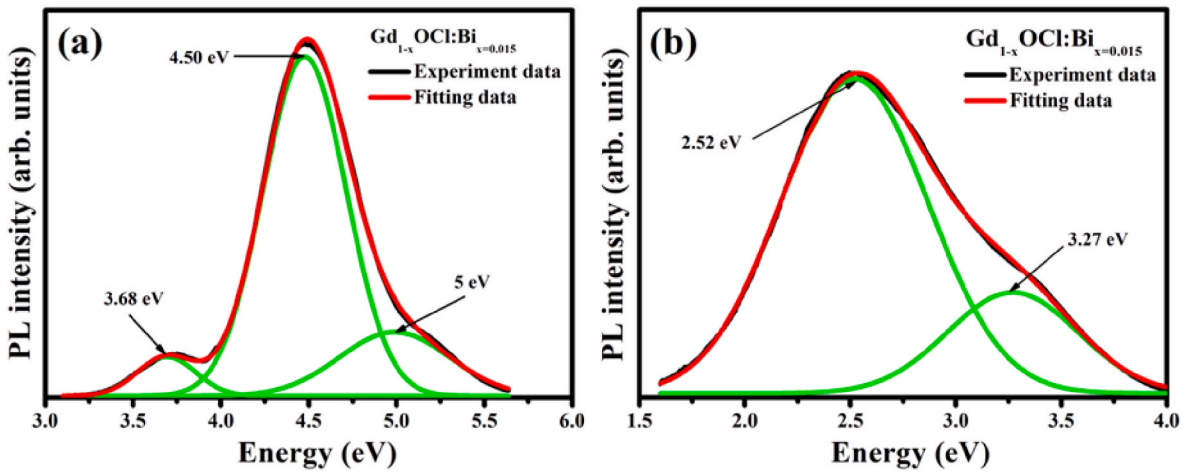

Fig. 12. Gaussian fitting of the $Gd_{1-x}OCl:Bi_{x\ =\ 0.015}$ (a) Excitation bands ($Em_{\lambda\ =\ 455\ nm}$) (b) emission bands excited by 275 nm.

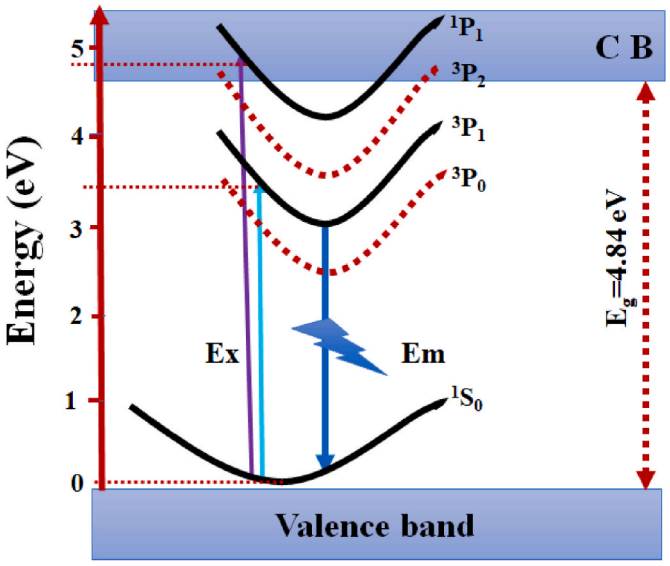

Fig. 13. Diagram illustrating the energy levels of the Bi^{3+} ion in GdOCl.

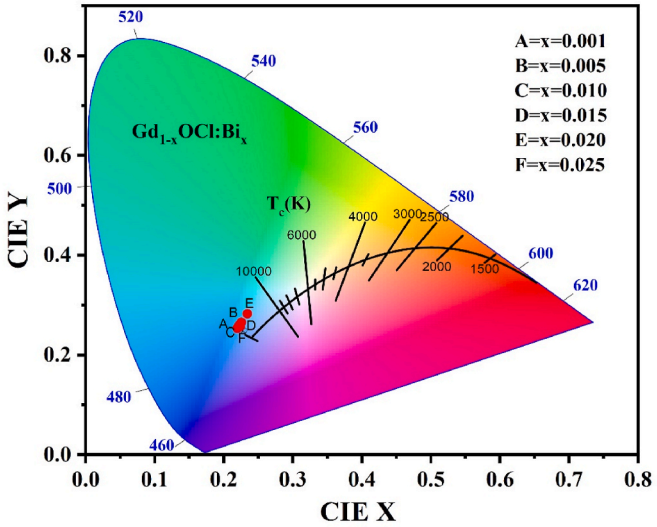

Fig. 14. CIE chromaticity diagram for $Gd_{1-x}OCl:Bi_x$.

values of the samples were determined within the range of 40957 K–55977 K, with varying concentrations of Bi ions. Light with higher correlated colour temperature (CCT) values, usually exceeding 5000 K, is characterized as cool blue light and is commonly linked with daylight or cool white lighting. On the other hand, CCT values below 5000 K are designated as warm blue light. A warmer blue light within this range might lean toward the lower end of the cool spectrum, approaching neutral white. While maintaining a blue undertone, it is not as distinctly pronounced as the cooler counterpart [42].

Assessing the colour purity of the prepared phosphor is a crucial step before considering its potential applications. The National Television System Committee (NTSC) and The European Broadcasting Union (EBU) have both underscored the importance of display phosphors meeting rigorous criteria with paramount stability and colour purity [43]. Consequently, one can ascertain colour purity by employing the following equation [43]:

$$\text{Colour purity} = \frac{\sqrt{(x-x_s)^2+(y-y_s)^2}}{\sqrt{(x_d-x_s)^2+(y_d-y_s)^2}} \times 100\% \quad (5)$$

The coordinates (x, y), (x_s, y_s), and (x_d, y_d) represent the coordinates corresponding to the sample, white light, and the dominant emission, respectively. The sample coordinates were extracted from Table 3, while the coordinates for white colour were sourced from the literature, specifically (0.3101, 0.3162) in the CIE 1930 colour space [43]. The computed colour purity and CCT values are shown in Tables 3 and it's noteworthy that the observed colour purity is relatively low, suggesting limited suitability for potential UV-LED applications. The data presented in Table 3 unequivocally demonstrate that phosphors with Gd_{1-x} $OCl:Bi_x$ composition (x = 0.001, 0.005, 0.010, 0.015, 0.020, and 0.025) exhibit an intense blue emission colour.

Fig. 15 illustrates the decay characteristics of $Gd_{1-x}OCl:Bi_x$ powder phosphors, all analysed utilizing a double exponential decay model. The mathematical representation for this model is as follows:

Table 3
CIE1931 chromaticity coordinates, correlated color temperature (CCT), and color purity values for $Gd_{1-x}OCl:Bi_x$.

Samples	CIE 1931 Coordinates x	y	CCT values (K)	color purity (%)
$Gd_{1-x}OCl:Bi_{x\ =\ 0.001}$	0.211	0.240	42320	38
$Gd_{1-x}OCl:Bi_{x\ =\ 0.005}$	0.211	0.234	50706	39
$Gd_{1-x}OCl:Bi_{x\ =\ 0.010}$	0.214	0.230	55977	39
$Gd_{1-x}OCl:Bi_{x\ =\ 0.015}$	0.215	0.235	46587	39
$Gd_{1-x}OCl:Bi_{x\ =\ 0.020}$	0.217	0.238	41491	36
$Gd_{1-x}OCl:Bi_{x\ =\ 0.025}$	0.218	0.238	40957	36

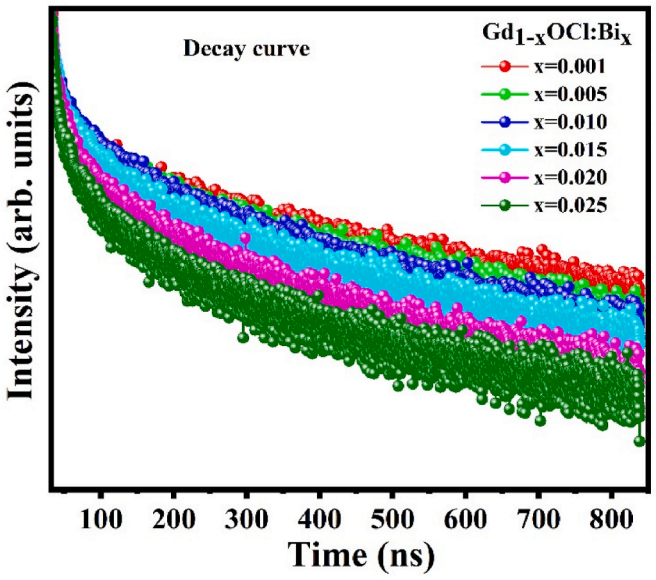

Fig. 15. Decay curves of $Gd_{1-x}OCl:Bi_x$ (x = 0.005–0.025) ($Ex_{\lambda=266\ nm}$, $Em_{\lambda=455\ nm}$).

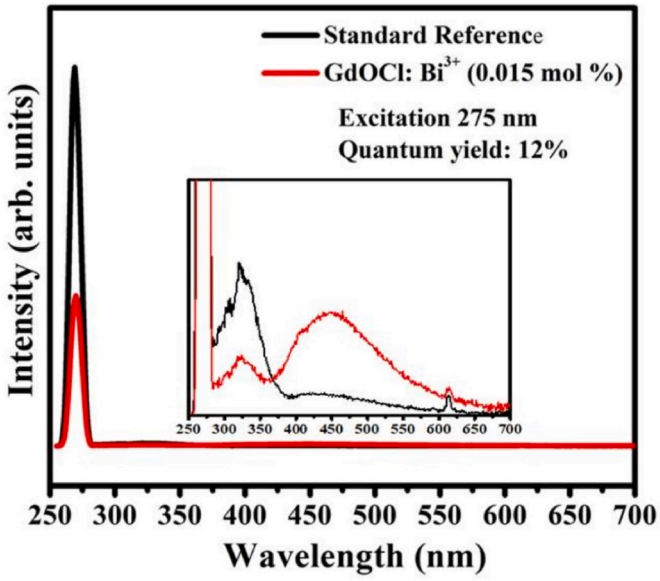

Fig. 16. Quantum yield measurement for $Gd_{1-x}OCl:Bi_{x\ =\ 0.015}$ sample under excitation of 275 nm using an integrating sphere.

$$I(t) = A^0 + A^1 \exp(-t/\tau^1) + A^2 \exp(-t/\tau^2) \quad (6)$$

in this equation, τ_1 and τ_2 signify the time constants for the rapid and slow decay components. A_0 represents the background signal, while A_1 and A_2 are the parameters used for fitting. To calculate the average lifetimes (τ_{ave}), the following equation was applied:

$$\tau_{ave} = \left(A^1\tau^{1(2)} + A^2\tau^{2(2)}\right) / \left(A^1\tau^1 + A^2\tau^2\right) \quad (7)$$

Table 4 contains the computed τ_{ave} values alongside the fitting data. Notably, as the concentration of Bi^{3+} dopant increases, the average lifetime decreases. As previously discussed, this occurrence can be ascribed to energy transfer among the Bi^{3+} ions, further contributing to the noted concentration quenching at elevated doping levels.

The PL quantum yield (η) for $Gd_{1-x}OCl:Bi_{x\ =\ 0.015}$ phosphor powder was determined using the FLS980 system, which was equipped with an integrating sphere, as illustrated in Fig. 16. The η represents the ratio of emitted photons (N^{em}) to absorbed photons (N^{ab}) and is given by the formula:

$$\eta = \frac{N^{em}}{N^{ab}} \quad (8)$$

For this analysis, the scatter and emission data were collected using the direct excitation method [44], and the absolute quantum yield (ηDE_{xc}) calculated by using the equation:

$$\eta DE_{xc} = \frac{E_B(\lambda) - E_A(\lambda)}{S_A(\lambda) - S_B(\lambda)} \quad (9)$$

Here, $E_B(\lambda)$ corresponds to the emission spectrum of the sample, $E_A(\lambda)$ is the emission spectrum of the reference, $S_A(\lambda)$ represents the scatter spectrum of the reference, and $S_B(\lambda)$ denotes the scatter spectrum of the sample. The quantum yield of the $Gd_{1-x}OCl:Bi_{x\ =\ 0.015}$ phosphor was determined to be 12 %. The measured quantum yield is relatively low compared to other oxyhalide systems doped with Bi^{3+}; for instance, YOF:Bi^{3+} has a quantum yield of about 60 % for UV emission [43]. This limits the utility of this prepared phosphor for optical applications.(See. Fig. 17)

Table 4
Fitting parameters and average lifetimes of $Gd_{1-x}OCl:Bi_x$.

Bi concentration (x)	A_1 (%)	τ_1 (ns)	A_2 (%)	τ_2 (ns)	τ_{ave} (ns)	χ^2
0.001	78	20	55	303	278	1.21
0.005	81	23	62	297	271	1.09
0.010	94	22	51	294	261	1.11
0.015	89	16	49	282	257	1.17
0.020	74	17	60	258	239	1.23
0.025	90	18	65	255	233	1.25

4. Conclusion

Using the solid-state reaction method, Bi-doped GdOCl was successfully synthesized. Analysis via XRD confirmed the tetragonal crystal structure of GdOCl. SEM imaging displayed a transformation in particle morphology from randomly oriented flat thin plates to nanorods upon Bi introduction into the GdOCl host matrix. The reflectance spectra of the doped samples displayed three distinct absorption bands: one at 215 nm, another at 257 nm, and a third at 336 nm. The 215 nm absorption band in the undoped sample signifies absorption above the material's band gap. The absorption band at 257 nm is attributed to Bi^{3+} ion absorption, while the 336 nm absorption may be linked to defects induced by Bi or the presence of Bi-clusters. Reflectance data analysis of the host material determined GdOCl's band gap, measured at 4.84 eV. Emission peaks at 428 nm and 455 nm were identified as originating from the $^3P_1 \rightarrow {}^1S_0$ transition of Bi^{3+} ions. A relatively weak emission at 495 nm was also associated with Bi clustering. It's important to note that GdOCl:Bi exhibited some structural instability when exposed to the atmosphere over an extended period of several months.

CRediT authorship contribution statement

Babiker M. Jaffar: Writing – original draft, Methodology, Investigation, Formal analysis, Data curation. **Nadir A.M. Saeed:** Data curation. **R.E. Kroon:** Writing – review & editing, Supervision, Resources, Formal analysis, Conceptualization. **Rudolph M. Erasmus:** Writing – review & editing, Resources, Formal analysis, Data curation. **Odireleng Martin Ntwaeaborwa:** Writing – review & editing, Validation, Supervision, Resources, Investigation, Formal analysis, Conceptualization.

Declaration of competing interest

The authors declare that they have no known competing financial interests or personal relationships that could have appeared to influence the work reported in this paper.

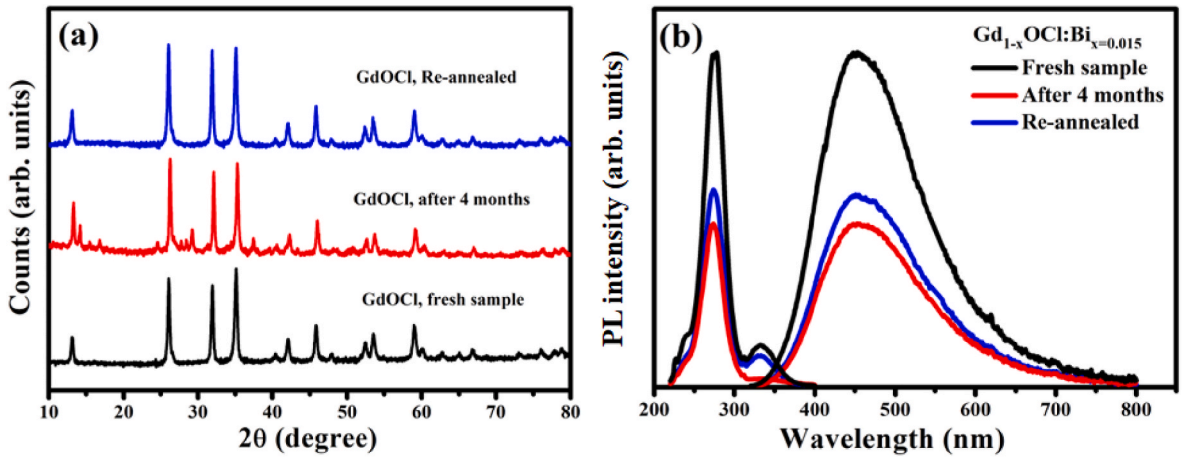

Fig. 17. (a) XRD patterns of freshly prepared $Gd_{1-x}OCl:Bi_{x=0.015}$, after 4 months exposure to the atmosphere and when re-annealed samples. (b) PL spectra for freshly prepared $Gd_{1-x}OCl:Bi_{x=0.015}$ powders initially, after 4 months, and re-annealed samples.

Data availability

Data will be made available on request.

References

[1] N. Dhananjaya, C. Shivakumara, Rohit Saraf, Sukanti Behera, H. Nagabhushana, Comparative study of Eu^{3+} activated LnOCl (Ln= La and Gd) phosphors and their Judd-Ofelt analysis, J. Rare Earths 33 (2015) 946–953, https://doi.org/10.1016/S1002-0721(14)60510-X.

[2] G.B. Nair, H.C. Swart, S.J. Dhoble, A review on the advancements in phosphor-converted light emitting diodes (pc-LEDs): phosphor synthesis, device fabrication, and characterization, Prog. Mater. Sci. 109 (2020) 100622, https://doi.org/10.1016/j.pmatsci.2019.100622.

[3] Q. Chen, Z. Feng, M.Z. Liu, B. Lou, C.-G. Mac, C.-K. Duan, The photoluminescence of isolated and paired Bi^{3+} ions in layered LnOCl crystals: a first-principles study, Phys. Chem. Chem. Phys. 24 (2022) 14064, https://doi.org/10.1039/d2cp01376b.

[4] M. Jaffar Babiker, H.C. Swart, H.A.A. Seed Ahmed, A. Yousif, R.E. Kroon, Comparative study of the luminescence of Bi-doped LaOCl and LaOBr phosphor powders, J. Lumin. 250 (2022) 119050, https://doi.org/10.1016/j.jlumin.2022.119050.

[5] Y. Li, X. Wei, M. Yin, Synthesis and upconversion luminescent properties of Er^{3+} doped and Er^{3+}–Yb^{3+} codoped GdOCl powders, J. Alloys Compd. 509 (2011) 9865–9868, https://doi.org/10.1016/j.jallcom.2011.07.060.

[6] J. Chen, Y. Song, D. Li, Q. Ma, X. Dong, W. Yu, Y. Yang, J. Wang, G. Liu, T. Wang, Dual-mode blue emission, paramagnetic properties of Yb^{3+}–Tm^{3+} co-doped GdOCl difunctional nanostructures, J. Mater. Sci. Mater. Electron. 28 (2017) 19038–19050, https://doi.org/10.1007/s10854-017-7858-6.

[7] Y. Li, Y. Pan, H. Chen, Y. Tao, VUV–UV luminescence of Ce^{3+}, Tb^{3+}, Eu^{3+}, and Dy^{3+} doped GdOCl, Opt. Mater. 50 (2015) 184–187, https://doi.org/10.1016/j.optmat.2015.10.019.

[8] S. Areva, J. Hölsä, R.-J. Lamminmäki, H. Rahiala, P. Dereń, W. Stręk, Excited state absorption processes in Sm^{3+} doped GdOCl, J. Alloys Compd. 300–301 (2000) 218–223, https://doi.org/10.1016/s0925-8388(99)00773-2.

[9] T.M. Kozhan, V.V. Kusnetsova, P.R. Pershukevich, I.I. Serqeev, V.S. Khomenko, Concentration dependence of IR luminescence quantum yield in GdOCl:Ho^{3+}, Spectrochim. Acta, Part A 55 (1999) 1407–1409, https://doi.org/10.1016/s1386-1425(98)00308-4.

[10] Y. Li, X. Wei, B. Tong, Y. Liu, Q. Zhang, W. Sun, M. Yin, Effect of Er^{3+} concentration on the upconversion luminescence of GdOCl:Er^{3+} powders with excitation of 514.5nm, Mater. Lett. 80 (2012) 184–186, https://doi.org/10.1016/j.matlet.2012.04.115.

[11] G. Blasse, A. Bril, Investigations on Bi^{3+} activated phosphors, J. Chem. Phys. 48 (1968) 217–222, https://doi.org/10.1063/1.1667905.

[12] L.I. Van Steensel, G. Blasse, The luminescence of Sb^{3+} in LaOCl, J. Alloys Compd. 232 (1996) 60–62, https://doi.org/10.1016/0925-8388(95)02017-9.

[13] A. Wolfert, G. Blasse, Luminescence of the Bi^{3+} ion in compounds LnOCl (ln = La, Y, Gd), Mater. Res. Bull. 19 (1984) 67–75, https://doi.org/10.1016/0025-5408(84)90011-4.

[14] Koichi Momma, Fujio Izumi, VESTA 3 for three-dimensional visualization of crystal, volumetric and morphology data, J. Appl. Crystallogr. 44 (2011) 1272–1276, https://doi.org/10.1107/S0021889811038970.

[15] G.R. Waetzig, G.A. Horrocks, J.W. Jude, L. Zuin, S. Banerjee, X-ray excited photoluminescence near the giant resonance in solid-solution $Gd_{1-x}Tb_xOCl$ nanocrystals and their retention upon solvothermal topotactic transformation to Gd_{1-x} Tb_xF_3, Nanoscale 8 (2016) 979–986, https://doi.org/10.1039/c5nr07819a.

[16] W.A.I. Tabaza, H.C. Swart, R.E. Kroon, Optical properties of Bi and energy transfer from Bi to Tb in $MgAl_2O_4$ phosphor, J. Lumin. 148 (2014) 192–197, https://doi.org/10.1016/j.jlumin.2013.12.018.

[17] H.P. Awater Roy, Pieter Dorenbos, The Bi^{3+} 6s and 6p electron binding energies in relation to the chemical environment of inorganic compounds, J. Lumin. 184 (2017) 221–231, https://doi.org/10.1016/j.jlumin.2016.12.021.

[18] R.D. Shannon, Revised effective ionic radii and systematic studies of interatomie distances in halides and chaleogenides, Acta Crystallogr. A 32 (1976) 751–767, https://doi.org/10.1107/S0567739476001551.

[19] V. Mote, Y. Purushotham, B. Dole, Williamson-Hall analysis in estimation of lattice strain in nanometer-sized ZnO particles, Journal of Theoretical and Applied Physics 6 (2012) 6, https://doi.org/10.1186/2251-7235-6-6.

[20] J. Rodríguez-Carvajal, Recent advances in magnetic structure determination by neutron powder diffraction, Phys. B Condens. Matter 192 (1993) 55–69, https://doi.org/10.1016/0921-4526(93)90108-i.

[21] X. Zhang, L. Chen, Q. Huang, H. Guo, Synthesis and upconversion properties of GdOBr:Er^{3+} phosphors, Mater. Res. Bull. 45 (2010) 1625–1627, https://doi.org/10.1016/j.materresbull.2010.07.008.

[22] H. 20 Guo, Y. Li, D. Wang, W. Zhang, M. Yin, L. Lou, S. Xia, Blue upconversion of cubic Gd_2O_3:Er produced by green laser, J. Alloys Compd. 376 (2004) 23–27, https://doi.org/10.1016/j.jallcom.2003.12.020.

[23] J. Hölsä, R.-J. Lamminmäki, M. Lastusaari, P. Porcher, Simulation of the Gd^{3+} energy level scheme in GdOCl, J. Alloys Compd. 323–324 (2001) 811–815, https://doi.org/10.1016/s0925-8388(01)01150-1.

[24] Rosendo López, Ricardo Gómez, Band-gap energy estimation from diffuse reflectance measurements on sol-gel and commercial TiO_2: a comparative study, J. Sol. Gel Sci. Technol. 61 (2012) 1–7, https://doi.org/10.1007/s10971-011-2582-9.

[25] Bingcheng Luo, Xiaohui Wang, Enke Tian, Hongzhou Song, Guowu Li, Longtu Li, Electronic, dielectric and optical properties of orthorhombic lanthanum gallate perovskite, J. Alloys Compd. 708 (2017) 187–193, https://doi.org/10.1016/j.jallcom.2017.02.267.

[26] Aman Pandey, Gunisha Jain, Divya Vyas, Silvia Irusta, Sudhanshu Sharma, Nonreducible, basic La_2O_3 to reducible, acidic $La_{2-x}Sb_xO_3$ with significant oxygen storage capacity, lower band gap, and effect on the catalytic activity, J. Phys. Chem. C 121 (2017) 481–489, https://doi.org/10.1021/acs.jpcc.6b10821.

[27] Qiaoling Chen, Zhaoyang Feng, MingZhe Liu, Bibo Lou, Chong-Geng Ma, Chang-Kui Duan, The photoluminescence of isolated and paired Bi^{3+} ions in layered LnOCl crystals: a first-principles study, Phys. Chem. Chem. Phys. 24 (22) (2022) 14064–14071, https://doi.org/10.1039/d2cp01376b.

[28] R.M. Jafer, H.C. Swart, A. Yousif, Vinod Kumar, E. Coetsee, The effect of annealing temperature on the luminescence properties of Y_2O_3 phosphor powders doped with a high concentration of Bi^{3+}, J. Lumin. 180 (2016) 198–203, https://doi.org/10.1016/j.jlumin.2016.08.042.

[29] Babiker M. Jaffar, H.C. Swart, H.A.A. Seed Ahmed, A. Yousif, R.E. Kroon, O. M. Ntwaeaborwa, Influence of doping concentration and annealing temperature on the structure, particle morphology, and luminescent properties of powders and pulsed laser deposited thin films of bismuth-doped lanthanum gallate, Opt. Mater. 143 (2023) 114291, https://doi.org/10.1016/j.optmat.2023.114291.

[30] A. Wolfert, G. Blasse, Luminescence of the Bi^{3+} ion in compounds LnOCl (ln = La, Y, Gd), Mater. Res. Bull. 19 (1984) 67–75, https://doi.org/10.1016/0025-5408(84)90011-4.

[31] R.T. Wegh, H. Donker, A. Meijerink, R.J. Lamminmäki, J. Hölsä, Vacuum-ultraviolet spectroscopy and quantum cutting forGd^{3+} in $LiYF_4$, Phys. Rev. B 56 (1997) 13841–13848, https://doi.org/10.1103/physrevb.56.13841.

[32] V.V. Shinde, R.G. Kunghatkar, S.J. Dhoble, UVB-emitting Gd^{3+}-activated M_2O_2S (where M = La, Y) for phototherapy lamp phosphors, Luminescence 30 (2015) 1257–1262, https://doi.org/10.1002/bio.2889.

[33] D.L. Dexter, James H. Schulman, Theory of concentration quenching in inorganic phosphors, J. Chem. Phys. 22 (1954) 1063–1070, https://doi.org/10.1063/1.1740265.
[34] Lili Wang, Qiang Sun, Qingzhi Liu, Jinsheng Shi, Investigation and application of quantitative relationship between sp energy levels of Bi^{3+}ion and host lattice, J. Solid State Chem. 191 (2012) 142–146, https://doi.org/10.1016/j.jssc.2012.03.015.
[35] Boutinaud Philippe, Revisiting the spectroscopy of the Bi^{3+} ion in oxide compounds, Inorg. Chem. 52 (2013) 6028–6038, https://doi.org/10.1021/ic400382k.
[36] M. Jaffar Babiker, H.C. Swart, H.A.A. Seed Ahmed, A. Yousif, R.E. Kroon, Comparative study of the luminescence of Bi-doped LaOCl and LaOBr phosphor powders, J. Lumin. 250 (2022) 119050, https://doi.org/10.1016/j.jlumin.2022.119050.
[37] N.A.M. Saeed, E. Coetsee, R.E. Kroon, M. Bettinelli, H.C. Swart, Photoluminescence of Bi^{3+} doped in YOF phosphor as an activator, Opt. Mater. 119 (2021) 111291, https://doi.org/10.1016/j.optmat.2021.111291.
[38] L. Li, S. Zhang, Dependence of charge transfer energy on crystal structure and composition in Eu^{3+}-doped compounds, J. Phys. Chem. B 110 (2006) 21438–21443, https://doi.org/10.1021/jp0552224.
[39] M. Amer, P. Boutinaud, On the character of the optical transitions in closed-shell transition metal oxides doped with Bi^{3+}, Phys. Chem. Chem. Phys. 19 (2017) 2591–2596, https://doi.org/10.1039/c6cp07638f.
[40] A.M. Srivastava, W.W. Beers, On the impurity trapped exciton luminescence in $La_2Zr_2O_7$:Bi^{3+}, J. Lumin. 81 (1999) 293–300, https://doi.org/10.1016/s0022-2313(99)00004-6.
[41] M. Monika, R.S. Yadav, A. Bahadur, S.B. Rai, Concentration and pump power-mediated color tunability, optical heating and temperature sensing via TCLs of red emission in an Er^{3+}/Yb^{3+}/Li^{+} co-doped $ZnGa_2O_4$ phosphor, RSC Adv. 9 (2019) 40092–40108, https://doi.org/10.1039/c9ra09120c.
[42] Semin Oh, Youngshin Kwak, A hue and warm-cool model for warm-cool based correlated color temperature calculation, Color Res. Appl. 47 (4) (2022) 953–965, https://doi.org/10.1002/col.22764.
[43] N.A.M. Saeed, E. Coetsee, H.C. Swart, Tunable Ho^{3+} co-doped YOF:Bi^{3+} emission through cathodoluminescence, Mater. Res. Bull. 159 (2023) 112089, https://doi.org/10.1016/j.materresbull.2022.112089.
[44] J.C. De Mello, H.F. Wittmann, R.H. Friend, An improved experimental determination of external photoluminescence quantum efficiency, Adv. Mater. 9 (1997) 230–232, https://doi.org/10.1002/adma.19970090308.